

Nonintrusive Manufactured Solutions for Non-Decomposing Ablation in Two Dimensions

Brian A. Freno^a, Brian R. Carnes^a, Victor E. Brunini^b, Neil R. Matula^a

^a*Sandia National Laboratories, Albuquerque, New Mexico 87185, USA*

^b*Sandia National Laboratories, Livermore, CA 94551, USA*

Abstract

Code verification is a necessary step towards establishing credibility in computational physics simulations. It is used to assess the correctness of the implementation of the numerical methods within the code, and it is a continuous part of code development. Code verification is typically performed using exact and manufactured solutions. However, exact solutions are often limited, and manufactured solutions generally require the invasive introduction of an artificial forcing term within the source code, such that the code solves a modified problem for which the solution is known. The equations for some physics phenomena, such as non-decomposing ablation, yield infinite analytic solutions, but the boundary conditions may eliminate these possibilities. For such phenomena, however, we can manufacture the terms that comprise the boundary conditions to obtain exact solutions. In this paper, we present a nonintrusive method for manufacturing solutions for non-decomposing ablation in two dimensions, which does not require the addition of a source term.

Keywords: code verification, manufactured solutions, ablation

1. Introduction

Ablation plays an important role in many scientific and engineering applications, including fire protection, surgical procedures, combustion, and manufacturing. An understanding of ablative processes is particularly critical in the realm of hypersonic flight, where the ablating material serves to carry heat energy away from the vehicle and its payload. Since weight and cost are paramount concerns for flight vehicles, accurate prediction of the rate of mass and energy removal is essential, as it allows the designer to minimize heat shield weight under the constraint of maintaining adequate thermal protection. Furthermore, the spatial distribution of the ablation process directly affects the aerodynamic performance of the vehicle. Hence, credible predictions of ablative processes are crucial for the design of safe and efficient high-speed vehicles.

As with the computational simulation of any physical phenomenon, it is necessary to assess the implementation and the suitability of the underlying models in order to develop confidence in the simulation results. These assessments typically fall into two complementary categories: verification and validation. Validation evaluates the appropriateness of the models instantiated in the code for representing the relevant physical phenomena, and is typically performed through comparison with experimental data. Verification, on the other hand, assesses the correctness of the numerical solutions produced by the code, through comparison with the expected theoretical behavior of the implemented numerical methods. Following Roache [1], Salari and Knupp [2], and Oberkampf and Roy [3], verification can be further divided into the activities of code verification and solution verification. Solution verification involves the estimation of the numerical error for a particular simulation, whereas code verification assesses the correctness of the implementation of the numerical methods within the code. A review of code and solution verification is presented by Roy [4].

This paper focuses on code verification. The discretization of the governing equations of the physical models necessarily incurs a truncation error, and the solution to the discretized equations therefore incurs an associated discretization error. In the most basic sense of verification, if the discretization error tends to zero as the discretization is refined, the consistency of the code is verified [1]. This may be taken a step

Email address: bafreno@sandia.gov (Brian A. Freno)

further by examining not only consistency, but the rate at which the error decreases as the discretization is refined. The code may then be verified by comparing this rate to the expected theoretical order of accuracy of the discretization scheme. Unfortunately, this approach requires knowledge of the exact solution to the problem at hand, and exact solutions to problems of engineering interest are rare. Hence, manufactured solutions are frequently employed to produce problems of sufficient complexity with known solutions [5].

Code verification is necessary to gather credibility evidence during the development of any simulation code that solves discretized equations. Examples of code verification have been demonstrated for computational physics codes associated with several physics disciplines, including fluid dynamics [6–11], solid mechanics [12], fluid–structure interaction [13], heat transfer in fluid–solid interaction [14], multiphase flows [15, 16], radiation hydrodynamics [17], electrodynamics [18], and electromagnetism [19–21]. Code-verification techniques for ablation have been presented by Hogan et al. [22], Blackwell and Hogan [23], and Amar et al. [24–26] for simple exact solutions. Additionally, a manufactured solution for heat conduction has been presented in Amar et al. [26]. A nonintrusive approach to manufactured solutions for non-decomposing ablation in one dimension has been introduced by Freno et al. [27].

For non-decomposing ablation, thermal decomposition is considered negligible. The governing equation is the heat equation with insulated boundaries on the non-ablating surfaces and a heat flux on the ablating surface that arises from convection, energy loss from ablation, and radiation.

In this paper, we extend the approach of Reference [27] to introduce a nonintrusive manufactured solutions approach for non-decomposing ablation in two dimensions, which introduces additional considerations, such as nontrivial mesh deformation and coordinate system choice. These nonintrusive manufactured solutions avoid the need to modify the code to introduce a forcing term. This property is particularly favorable for cases where the code is either proprietary or has other characteristics that make it inaccessible to one performing code verification. The trade-off is reduced freedom compared to traditional manufactured solutions; however, this reduction does not limit the ability to exercise the capabilities of the code.

This approach is designed for equations with complicated boundary conditions. For non-decomposing ablation and other physics phenomena with governing equations that permit analytic solutions, this approach avoids the need to modify the code to introduce a forcing term. However, for other phenomena, such as decomposing ablation, analytic solutions require too many limiting assumptions, and a forcing term needs to be introduced. For these phenomena, after manufacturing the solution, the parameters can be manufactured to satisfy the boundary conditions.

For non-decomposing ablation, we begin this process by optionally transforming the governing equations and deriving solutions to them. These solutions satisfy the boundary conditions on the non-ablating surfaces but not on the ablating surface. With these solutions, we manufacture the remaining parameters to satisfy the boundary condition on the ablating surface. Like traditional manufactured solutions, certain desirable properties of the underlying functions, such as a sufficient number of finite nontrivial derivatives and elementary function composition, take precedence over being physically realizable. Through this approach we can modify external data, rather than modifying the code to introduce a forcing term.

This paper is organized as follows. Section 2 describes the heat equation, as well as the ablation contribution and the domain evolution. Section 3 details our approach for verifying the accuracy of the discretization. Section 4 provides derivations of exact solutions to the heat equation to account for ablation in Cartesian and polar coordinates. Section 5 describes how the ablation parameters are manufactured to satisfy the boundary conditions. Section 6 demonstrates this methodology with numerical examples. Section 7 summarizes this work.

2. Governing Equations

For a solid, the energy equation due to heat conduction is

$$\frac{\partial}{\partial t}(\rho e) + \nabla \cdot \mathbf{q} = 0. \quad (1)$$

The specific internal energy e can be modeled by $e = e_0 + \int_{T_0}^T c_p(\hat{T})d\hat{T}$, where $c_p = c_p(T)$ is the specific heat capacity, and the heat flux \mathbf{q} can be modeled by Fourier’s law,

$$\mathbf{q} = -k(T)\nabla T, \quad (2)$$

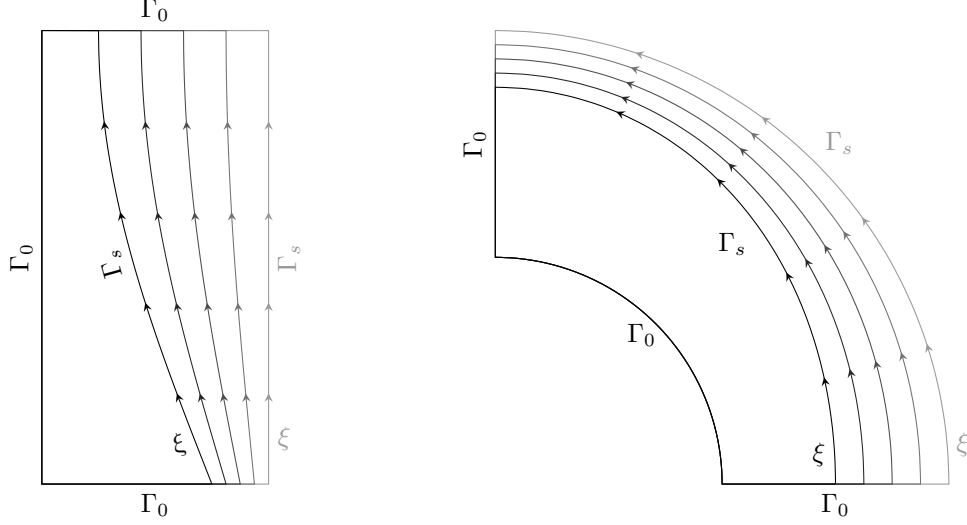


Figure 1: The boundary Γ of the domain consists of an ablating surface Γ_s and a non-ablating surface Γ_0 , such that $\Gamma = \Gamma_s \cup \Gamma_0$. Γ_s is parameterized by $\xi \in [0, 1]$, which increases in the counterclockwise direction.

where $k(T)$ is the thermal conductivity of the isotropic material.

If the material density ρ is constant, (1) becomes

$$\rho c_p(T) \frac{\partial T}{\partial t} - \nabla \cdot (k(T) \nabla T) = 0. \quad (3)$$

When the material properties are constants, such that $k = \bar{k}$ and $c_p = \bar{c}_p$, (3) reduces to the constant-coefficient heat equation, $\frac{\partial T}{\partial t} - \bar{\alpha} \Delta T = 0$, with thermal diffusivity $\bar{\alpha} = \frac{\bar{k}}{\rho \bar{c}_p}$.

2.1. Ablation and Boundary Conditions

We denote the time-dependent domain of the material by $\Omega(t)$. The boundary Γ of the domain consists of an ablating surface Γ_s and a non-ablating surface Γ_0 , such that $\Gamma = \Gamma_s \cup \Gamma_0$. We denote the ablating surface by $\Gamma_s = \{(x, y) : x = x_s, y = y_s\}$, which is arbitrarily parameterized by $\mathbf{x}_s(\xi, t) = (x_s(\xi, t), y_s(\xi, t))$, where $\xi \in [0, 1]$ increases in the counterclockwise direction, and $t \in [0, \bar{t}]$, with \bar{t} denoting the final time. Figure 1 shows examples of Γ and ξ .

Along the ablating surface Γ_s , the material recedes by an amount $s(\xi, t)$ in the direction opposite to the outer normal of the surface, such that the recession rate is defined by

$$\dot{s}(\xi, t) = -\frac{\partial \mathbf{x}_s}{\partial t}(\xi, t) \cdot \mathbf{n}_s(\xi, t), \quad (4)$$

where the outer unit normal vector is defined by

$$\mathbf{n}_s(\xi, t) = \frac{1}{\sqrt{(\partial x_s / \partial \xi)^2 + (\partial y_s / \partial \xi)^2}} \frac{\partial}{\partial \xi} \begin{Bmatrix} y_s \\ -x_s \end{Bmatrix}. \quad (5)$$

The recession rate is modeled by

$$\dot{s}(\xi, t) = \frac{B'(T_s, p_e) C_e}{\rho}, \quad (6)$$

where $T_s(\xi, t) = T(\mathbf{x}_s(\xi, t), t)$ is the temperature of the solid along the ablating surface, $p_e(\xi, t)$ is the pressure at the outer edge of the boundary layer expressed in terms of position along the ablating surface, and $B'(T_s, p_e)$ is the nondimensionalized char ablation rate. The heat transfer coefficient, $C_e(\xi, t)$, is commonly

denoted by $\rho_e u_e C_h$, where C_h is the Stanton number and ρ_e and u_e are the density and velocity at the outer edge of the boundary layer [24].

Defining $q_s = \mathbf{q}_s \cdot \mathbf{n}_s$, the heat flux normal to the ablating surface is

$$q_s = C_e [h_w(T_s, p_e) - h_r] + \rho \dot{s} [h_w(T_s, p_e) - h_s(T_s)] + \epsilon \sigma (T_s^4 - T_r^4). \quad (7)$$

In (7), the first term is the convective heat flux, the second term is the energy loss from ablation, and the third term is the radiative flux. $h_w(T_s, p_e)$ is the wall enthalpy and $h_r(\xi, t)$ is the recovery enthalpy. $h_s(\xi, t)$ is the solid enthalpy, computed from

$$h_s(T_s) = h_0 + \int_{T_0}^{T_s} c_p(\hat{T}) d\hat{T}, \quad (8)$$

where, for our purposes, we set $h_0 = 0$ J/kg and $T_0 = 273.15$ K. ϵ is the emissivity, σ is the Stefan–Boltzmann constant, and T_r is a radiation reference temperature, which we set to $T_r = 300$ K. $B'(T_s, p_e)$ in (6) and $h_w(T_s, p_e)$ in (7) are both computed from a surface thermochemistry model and provided as tabulated data, and ϵ in (7) is modeled as a constant.

From (2) and referencing (7), the boundary condition along the ablating surface is

$$-k(T_s) \frac{\partial T}{\partial n} = q_s. \quad (9)$$

The non-ablating surface Γ_0 is insulated, such that there is no heat flux ($q_0 = \mathbf{q}_0 \cdot \mathbf{n}_0 = 0$), and, from (2),

$$\frac{\partial T}{\partial n} = 0. \quad (10)$$

3. Manufactured Solutions

A governing system of partial differential equations can be written generally as

$$\mathbf{r}(\mathbf{u}; \boldsymbol{\mu}) = \mathbf{0}, \quad (11)$$

where $\mathbf{r}(\mathbf{u}; \boldsymbol{\mu})$ is a symbolic operator representing the governing equations, $\mathbf{u} = \mathbf{u}(\mathbf{x}, t)$ is the state vector, and $\boldsymbol{\mu}$ is the parameter vector. To solve (11) numerically, it must be discretized in time and space:

$$\mathbf{r}_h(\mathbf{u}_h; \boldsymbol{\mu}) = \mathbf{0},$$

where \mathbf{r}_h is the residual of the discretized system of equations, and \mathbf{u}_h is the solution to the discretized equations.

There is an a priori error estimate for the discretization error $\mathbf{e}_u = \mathbf{u}_h - \mathbf{u}$ and its norm, which asymptotically has the form $\|\mathbf{e}_u\| \approx Ch^p$, where C is a function of the solution derivatives, h is representative of the discretization size, and p is the order of accuracy. Through convergence studies of the norm of the error, we can assess whether the expected order of accuracy is obtained.

However, \mathbf{e}_u can only be measured if \mathbf{u} is known. Exact solutions to (11) require negligible implementation effort, but are generally too limited to fully exercise the capabilities of the code. Manufactured solutions are therefore popular alternatives, which typically introduce a forcing vector into the original equations to coerce the solution to the manufactured one:

$$\mathbf{r}_h(\mathbf{u}_h; \boldsymbol{\mu}) = \mathbf{r}(\mathbf{u}_{\text{MS}}; \boldsymbol{\mu}). \quad (12)$$

In (12), $\mathbf{r}(\mathbf{u}_{\text{MS}}; \boldsymbol{\mu})$ is computed analytically since \mathbf{r} , \mathbf{u}_{MS} , and $\boldsymbol{\mu}$ are known. To simplify the notation, we have assumed the appropriate mapping of $\mathbf{r}(\mathbf{u}_{\text{MS}}; \boldsymbol{\mu})$ onto the discrete space, where it is evaluated.

An alternative approach, which we employ in this paper, involves manufacturing the parameters instead to obtain $\mathbf{r}(\mathbf{u}; \boldsymbol{\mu}_{\text{MP}}) = \mathbf{0}$, which is solved numerically by

$$\mathbf{r}_h(\mathbf{u}_h; \boldsymbol{\mu}_{\text{MP}}) = \mathbf{0}. \quad (13)$$

Unlike the approach in (12), the approach in (13) does not require code modification.

To compute \mathbf{u} , we derive solutions to the governing equations. For the boundary conditions that cannot be satisfied, we manufacture the underlying parameters $\boldsymbol{\mu}_{\text{MP}}$. For ablation, we demonstrate this approach in Sections 4 and 5.

4. Heat Equation Solution

We consider the temperature-dependent material properties $k(T) = \bar{k}f(T)$ and $c_p(T) = \bar{c}_p f(T)$, where $f(T) > 0$ for $T > 0$. Employing a Kirchhoff transformation,

$$\theta(\mathbf{x}, t) = \frac{1}{\bar{k}} \int_T k(T') dT' + C_k = \int_T f(T') dT' + C_k = F(T), \quad (14)$$

where θ denotes the transformed temperature, we obtain

$$\begin{aligned} \frac{\partial \theta}{\partial t} &= f(T) \frac{\partial T}{\partial t}, \\ \nabla \theta &= f(T) \nabla T, \end{aligned} \quad (15)$$

which are substituted into (3) to yield a constant-coefficient heat equation

$$\frac{\partial \theta}{\partial t} - \bar{\alpha} \Delta \theta = 0. \quad (16)$$

From (15), the normal derivatives are related by

$$\frac{\partial T}{\partial n} = \frac{1}{f(T)} \frac{\partial \theta}{\partial n}. \quad (17)$$

While a constant thermal diffusivity significantly simplifies the solution to the heat equation, limited analytic solutions can be obtained from other functional forms for k and c_p . Nonetheless, because $f(T)$ permits k and c_p to vary with T and test that capability of the code, we restrict k and c_p to these forms.

To solve (16), we temporarily disregard the time dependency of the domain due to the ablating surface and assume we can separate the time and space dependencies of the solution, such that

$$\theta(\mathbf{x}, t) = \sum_{i=0}^{\infty} \sum_{j=0}^{\infty} \hat{\theta}_{i,j}(t) \varphi_{i,j}(\mathbf{x}), \quad (18)$$

where $\varphi_{i,j}(\mathbf{x})$ is an orthogonal basis, and i and j are indices associated with the basis of different spatial coordinates. Substituting (18) into (16) yields

$$\frac{1}{\bar{\alpha}} \frac{\hat{\theta}'_{i,j}(t)}{\hat{\theta}_{i,j}(t)} = \frac{\Delta \varphi_{i,j}(\mathbf{x})}{\varphi_{i,j}(\mathbf{x})} = -\lambda_{i,j}. \quad (19)$$

From (19),

$$\hat{\theta}_{i,j}(t) = \hat{\theta}_{i,j_0} e^{-\bar{\alpha} \lambda_{i,j} t}, \quad (20)$$

where

$$\hat{\theta}_{i,j_0} = \frac{\int_{\Omega(0)} \theta(\mathbf{x}, 0) \varphi_{i,j}(\mathbf{x}) d\Omega}{\int_{\Omega(0)} \varphi_{i,j}(\mathbf{x})^2 d\Omega}.$$

Because we are focusing on ablative processes and interested in verifying the time integrator, we are particularly interested in cases where the temperature increases with time, which occurs when $\lambda_{i,j} < 0$.

In the following two subsections, we derive $\varphi_{i,j}(\mathbf{x})$ and $\lambda_{i,j}$ for 1) a particular type of domain in Cartesian coordinates, and 2) a particular type of domain in polar coordinates.

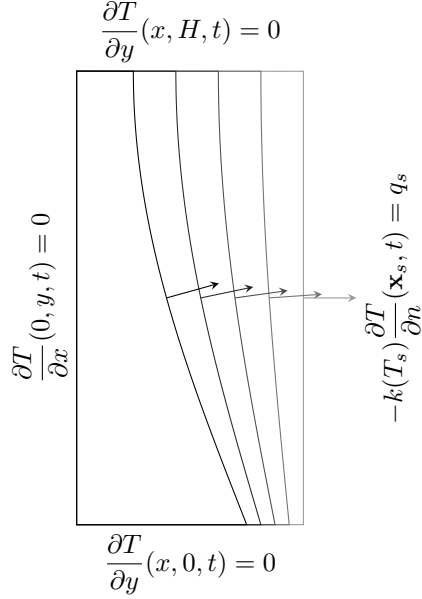


Figure 2: Domain and boundary conditions in Cartesian coordinates.

4.1. Cartesian Coordinates

For this problem, the domain is defined by $\Omega = \{(x, y) : 0 \leq x \leq x_s(y), 0 \leq y \leq H\}$. The ablating surface Γ_s is subject to the boundary condition in (9), whereas the remaining edges ($x = 0, y = 0, y = H$) comprise Γ_0 , with the boundary condition in (10). Figure 2 provides an example of this domain; however, it is not necessary for the domain to initially be a rectangle. The requirement is that the three edges that comprise Γ_0 remain straight, with the middle edge perpendicular to the mutually parallel remaining edges.

With this requirement, we assume we can separate the x and y dependencies, such that

$$\varphi_{i,j}(\mathbf{x}) = u_i(x)v_j(y). \quad (21)$$

From (19), we obtain

$$\lambda_{i,j} + \frac{u_i''(x)}{u_i(x)} = -\frac{v_j''(y)}{v_j(y)} = \nu_j^2. \quad (22)$$

From (22), $v_j''(y) + \nu_j^2 v_j(y) = 0$, and from (10) and (17), at $y = 0$ and $y = H$, $\frac{\partial \theta}{\partial y} = 0$, such that $v_j'(0) = v_j'(H) = 0$. For a nontrivial solution for v_j , $\nu_j = j\pi/H$ for $j \in \mathbb{N}_0$, such that

$$v_j(y) = \cos(j\pi y/H). \quad (23)$$

From (22), $u_i''(x) + \mu_i^2 u_i(x) = 0$, where $\mu_i^2 = \lambda_{i,j} - \nu_j^2$, and μ_i^2 is real. From (10) and (17), at $x = 0$, $\frac{\partial \theta}{\partial x} = 0$, such that $u_i'(0) = 0$. For a nontrivial solution for u_i ,

$$u_i(x) = \begin{cases} \cosh(|\mu_i|x) & \text{for } \mu_i^2 < 0 \\ \cos(\mu_i x) & \text{for } \mu_i^2 \geq 0 \end{cases}, \quad (24)$$

where μ_i depends on the boundary condition at $x = x_s$.

With $\varphi_{i,j}(\mathbf{x})$ (21) and

$$\lambda_{i,j} = \mu_i^2 + \nu_j^2 \quad (25)$$

known, (18) satisfies (16) and the boundary conditions on Γ_0 (10). However, the boundary condition on Γ_s (9) has not been addressed and μ_i has not been determined. Because the domain varies with respect to time and x_s can vary with respect to y , we cannot satisfy general boundary conditions with (18). Therefore, in Section 5, we manufacture the ablating boundary condition such that it is always satisfied.

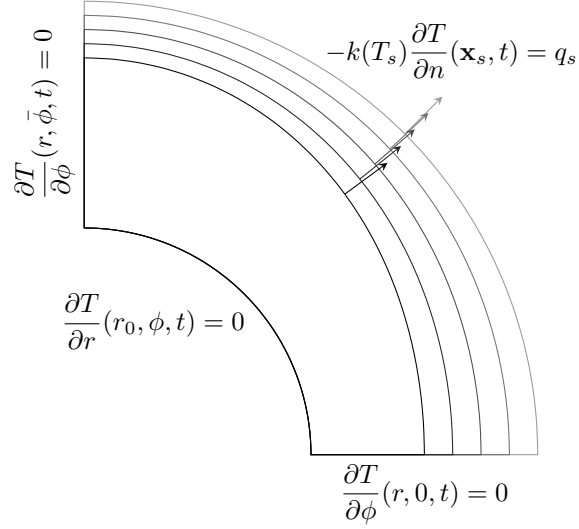


Figure 3: Domain and boundary conditions in polar coordinates.

4.2. Polar Coordinates

For this problem, the domain is defined by $\Omega = \{(r, \phi) : r_0 \leq r \leq r_s(\phi), 0 \leq \phi \leq \bar{\phi}\}$. The ablating surface Γ_s is subject to the boundary condition in (9), whereas the remaining edges ($r = r_0, \phi = 0, \phi = \bar{\phi}$) comprise Γ_0 , with the boundary condition in (10). Figure 3 provides an example of this domain with $\bar{\phi} = \pi/2$; however, it is not necessary for the domain to initially be a fractional annulus. The requirements are that the two radial edges that comprise Γ_0 remain radial at fixed angles, and the inner edge remains a circular arc.

With these requirements, we assume we can partially separate the r and ϕ dependencies, such that

$$\varphi_{i,j}(\mathbf{x}) = u_{i,j}(r)v_j(\phi).$$

Note that, unlike $u_i(x)$ and $v_j(y)$, which are decoupled in Section 4.1, $u_{i,j}(r)$ depends on $v_j(\phi)$. From (19), we obtain

$$\lambda_{i,j}r^2 + \frac{r^2u''_{i,j}(r) + ru'_{i,j}(r)}{u_{i,j}(r)} = -\frac{v''_j(\phi)}{v_j(\phi)} = \nu_j^2. \quad (26)$$

From (26), $v''_j(\phi) + \nu_j^2v_j(\phi) = 0$, and from (10) and (17), at $\phi = 0$ and $\phi = \bar{\phi}$, $\frac{\partial \theta}{\partial \phi} = 0$, such that $v'_j(0) = v'_j(\bar{\phi}) = 0$. For a nontrivial solution for v_j , $\nu_j = j\pi/\bar{\phi}$ for $j \in \mathbb{N}_0$, such that

$$v_j(\phi) = \cos(j\pi\phi/\bar{\phi}). \quad (27)$$

From (26), we obtain

$$r^2u''_{i,j}(r) + ru'_{i,j}(r) + (\lambda_{i,j}r^2 - \nu_j^2)u_{i,j}(r) = 0,$$

and from (10) and (17), at $r = r_0$, $\frac{\partial \theta}{\partial r} = 0$, such that $u'_{i,j}(r_0) = 0$. For a nontrivial solution for $u_{i,j}$,

$$u_{i,j}(r) = \begin{cases} K_{i,j}I_{\nu_j}(r') + I_{i,j}K_{\nu_j}(r') & \text{for } \lambda_{i,j} < 0 \\ Y_{i,j}J_{\nu_j}(r') + J_{i,j}Y_{\nu_j}(r') & \text{for } \lambda_{i,j} > 0, \\ \cosh(\nu_j \ln(r/r_0)) & \text{for } \lambda_{i,j} = 0 \end{cases} \quad (28)$$

where $r' = \sqrt{|\lambda_{i,j}|}r$, I_α and K_α are modified Bessel functions of the first and second kind [28], J_α and Y_α are Bessel functions of the first and second kind, and

$$\begin{aligned} K_{i,j} &= K_{\nu_j-1}(r'_0) + K_{\nu_j+1}(r'_0), \\ I_{i,j} &= I_{\nu_j-1}(r'_0) + I_{\nu_j+1}(r'_0), \\ Y_{i,j} &= Y_{\nu_j-1}(r'_0) - Y_{\nu_j+1}(r'_0), \\ J_{i,j} &= -J_{\nu_j-1}(r'_0) + J_{\nu_j+1}(r'_0). \end{aligned}$$

$\lambda_{i,j}$ depends on the boundary condition at $r = r_s$.

As with Section 4.1, the boundary condition on Γ_s (9) has not yet been addressed and $\lambda_{i,j}$ has not been determined. In Section 5, we manufacture the ablating boundary condition such that it is always satisfied.

5. Boundary Condition Reconciliation

In this section, we manufacture the ablating boundary condition so that we can manufacture solutions without adding a source term. In doing so, we have much freedom, provided the functions are sufficiently smooth. Like traditional manufactured solutions, certain desirable properties of the underlying functions, such as a sufficient number of finite nontrivial derivatives and elementary function composition, take precedence over being physically realizable.

We begin by manufacturing $T(\mathbf{x}, t)$, which requires manufacturing the material properties $k(T)$, $c_p(T)$, and ρ , as well as $\theta(\mathbf{x}, t)$ (18).

To manufacture the material properties, we must manufacture \bar{k} , \bar{c}_p , ρ , and ϵ , as well as $f(T)$. From \bar{k} , \bar{c}_p , and ρ , we can compute $\bar{\alpha}$ in (20). $f(T)$ relates $\theta(\mathbf{x}, t)$ and $T(\mathbf{x}, t)$ and provides the dependencies of $k(T)$ and $c_p(T)$ on T ; it should be manufactured such that the inverse of (14), $T(\mathbf{x}, t) = F^{-1}(\theta)$, can be easily computed.

To manufacture $\theta(\mathbf{x}, t)$, we truncate the series in (18) and we specify $\hat{\theta}_{i,j_0}$ in $\hat{\theta}_{i,j}(t)$ (20). If we are using Cartesian coordinates, we specify μ_i , which appears in $u_i(x)$ (24) and $\lambda_{i,j}$ (25). If we are using polar coordinates, we specify $\lambda_{i,j}$. With $\theta(\mathbf{x}, t)$ specified, we can compute the temperature from $T(\mathbf{x}, t) = F^{-1}(\theta)$.

Next, we manufacture $\mathbf{x}_s(\xi, t)$, such that we can compute $\mathbf{n}_s(\xi, t)$ from (5), then $\dot{s}(\xi, t)$ from (4).

With $T(\mathbf{x}, t)$ and $\mathbf{x}_s(\xi, t)$ manufactured, the next step is to manufacture the parameters to satisfy the boundary condition on Γ_s (9):

$$q_s = -k(T_s) \frac{\partial T}{\partial n} = C_e [h_w(T_s, p_e) - h_r] + \rho \dot{s} [h_w(T_s, p_e) - h_s(T_s)] + \epsilon \sigma (T_s^4 - T_r^4), \quad (29)$$

as well as the recession rate (6). In (29), $k(T_s)$, T_s , $\frac{\partial T}{\partial n}$, ρ , and $\dot{s}(\xi, t)$ have already been determined, and $h_s(\xi, t) = h_s(T_s(\xi, t))$ can be computed from (8) using $T(\mathbf{x}, t)$, $\mathbf{x}_s(\xi, t)$, and $c_p(T)$. Therefore, $C_e(\xi, t)$, $p_e(\xi, t)$, $h_w(T_s, p_e)$, and $h_r(\xi, t)$ need to be determined. In (6), $\dot{s}(\xi, t)$ has already been determined, such that $B'(T_s, p_e)$ and $C_e(\xi, t)$ need to be determined. Therefore, we next manufacture $B'(T_s, p_e)$ and $p_e(\xi, t)$.

Using (6), (29) can be written as

$$q_s = C_e (h_w(T_s, p_e) [1 + B'(T_s, p_e)] - h_r - B'(T_s, p_e) h_s(T_s)) + \epsilon \sigma (T_s^4 - T_r^4). \quad (30)$$

In manufacturing the parameters, care must be taken to ensure that (30) does not introduce instabilities due to perturbations in the temperature, such as those that arise from discretization errors. Therefore, as explained in Appendix A, we impose $\frac{\partial q_s}{\partial T_s} \geq 0$. In (30),

$$\frac{\partial}{\partial T_s} [\epsilon \sigma (T_s^4 - T_r^4)] = 4\epsilon \sigma T_s^3 \geq 0.$$

Therefore, $\frac{\partial q_s}{\partial T_s} \geq 0$ will be satisfied if we set

$$\frac{\partial}{\partial T_s} [C_e (h_w(T_s, p_e) [1 + B'(T_s, p_e)] - h_r - B'(T_s, p_e) h_s(T_s))] = 0,$$

which yields

$$h_w(T_s, p_e)[1 + B'(T_s, p_e)] - B'(T_s, p_e)h_s(T_s) = g(p_e),$$

such that

$$h_w(T_s, p_e) = \frac{B'(T_s, p_e)h_s(T_s) + g(p_e)}{1 + B'(T_s, p_e)}.$$

For convenience, we set $g(p_e) = 0$. With these functions known, we compute $C_e(\xi, t)$ from (6) and $h_r(\xi, t)$ from (29).

6. Numerical Examples

In this section, we demonstrate the methodology of Section 5 on problems in Cartesian and polar coordinate systems using **SIERRA Multimechanics Module: Aria** [29] for multiple discretizations. The spatial domain is discretized using second-order-accurate finite elements, and the equations are integrated in time using a first-order-accurate backward Euler scheme. Therefore, each subsequent discretization uses twice the number of elements in each spatial dimension and a quarter of the time step size as the previous discretization. Additionally, the piecewise linear interpolation of tabulated parameters is second-order accurate, such that, for each discretization, we halve the spacing between the data samples. Letting h denote a quantity inversely proportional to the number of elements in one dimension and proportional to the square root of the time step size and accounting for the aforementioned refinement ratios, we expect the error to be $\mathcal{O}(h^2)$.

We measure the error in the temperature using the norm

$$\varepsilon_T = \max_{t \in [0, \bar{t}]} \|T_h(\mathbf{x}, t) - T(\mathbf{x}, t)\|_2, \quad (31)$$

by taking maximum over the time steps of the L^2 -norm of the error over the spatial domain. The subscript h denotes the solution to the discretized equations. We similarly measure the error in the ablating surface using the norm

$$\varepsilon_{\mathbf{x}_s} = \max_{t \in [0, \bar{t}]} \|\mathbf{x}_{s_h}(\xi, t) - \mathbf{x}_s(\xi, t)\|_2. \quad (32)$$

In (32), the L^2 -norm of the error is computed over the ablating surface.

Mesh deformation is accomplished through a Gent hyperelastic mesh stress model [30].

For both problem sets, we consider cases with ($\epsilon = 0.9$) and without ($\epsilon = 0$) the radiative flux. For the material properties, we consider $\bar{\alpha} = \{10^{-8}, 10^{-7}, 10^{-6}, 10^{-5}\}$ m²/s, $\rho = 1000$ kg/m³, and $\bar{k} = 0.7$ W/m/K, which enable us to compute \bar{c}_p . The multiple $\bar{\alpha}$ values enable us to consider different relative weights between the spatial and temporal contributions to the discretization error as we assess its convergence rate. For the thermochemical data, we manufacture

$$B'(T_s, p_e) = \exp\left(\frac{1}{1000} \frac{T_s}{\bar{T}} - \frac{1}{50} \frac{p_e}{\bar{p}}\right),$$

where $\bar{T} = 1$ K, $p_e(t) = \bar{p}e^{5t/\bar{t}}/200$, $\bar{p} = 101,325$ Pa, and $\bar{t} = 5$ s.

6.1. Cartesian Coordinates

The first problem set we consider uses Cartesian coordinates. For the temperature dependence, we choose

$$f(T) = \frac{4}{3} \left(\frac{T}{\bar{T}}\right)^{1/3},$$

such that $\theta(\mathbf{x}, t) = F(T) = (T(\mathbf{x}, t)^4/\bar{T})^{1/3}$ and $T(\mathbf{x}, t) = F^{-1}(\theta) = (\bar{T}\theta(\mathbf{x}, t)^3)^{1/4}$.

For $\theta(\mathbf{x}, t)$, we truncate (18) to $\max i = 0$ and $\max j = 1$. We choose this truncation because, from (23), $v_0(y) = 1$ and $v_1(y) = \cos(\pi y/H)$ enable us to obtain variation with respect to y without $\theta(\mathbf{x}, t)$ becoming

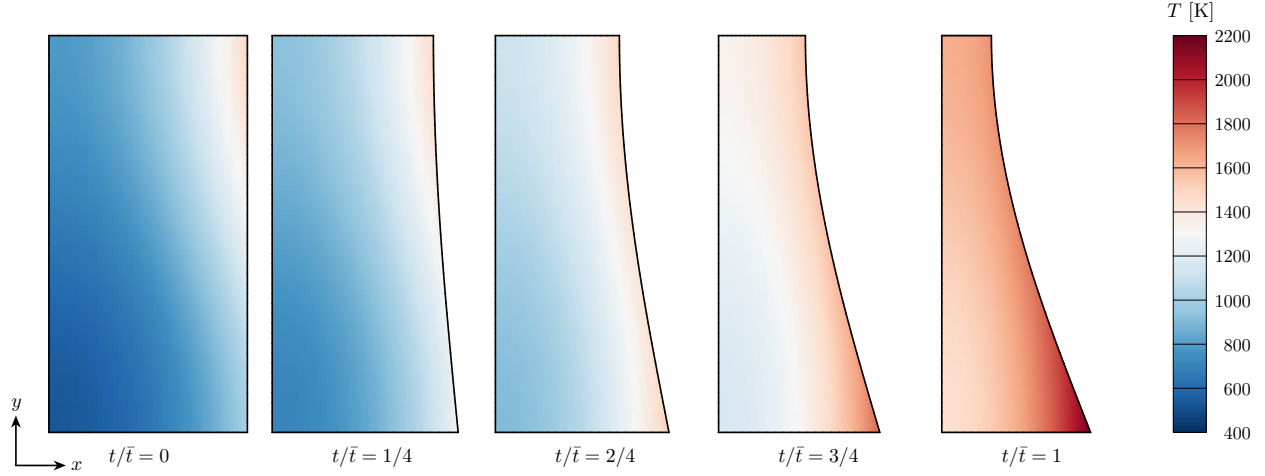


Figure 4: Cartesian coordinates: Temperature at multiple instances in time for $\bar{\alpha} = 10^{-5} \text{ m}^2/\text{s}$.

$\bar{\alpha} \text{ [m}^2/\text{s]}$	$T_s \text{ [}\times 10^3 \text{ K]}$		$c_p(T_s) \text{ [J/kg/K]}$		$k(T_s) \text{ [}\times 10^{-1} \text{ W/m/K]}$	
	Min.	Max.	Min.	Max.	Min.	Max.
10^{-8}	0.7255	1.4864	5.8150×10^4	7.3855×10^4	5.8150	7.3855
10^{-7}	0.7322	1.4864	5.8328×10^3	7.3855×10^3	5.8328	7.3855
10^{-6}	0.8006	1.4864	6.0089×10^2	7.3855×10^2	6.0089	7.3855
10^{-5}	1.0133	2.1674	6.5000×10^1	8.3749×10^1	6.5000	8.3749

Table 1: Cartesian coordinates: Extrema of T_s , $c_p(T_s)$, and $k(T_s)$ for $t \in [0, \bar{t}]$.

$\bar{\alpha} \text{ [m}^2/\text{s]}$	$h_s(T_s) \text{ [J/kg]}$		$h_w(T_s, p_e) \text{ [J/kg]}$		$B'(T_s, p_e)$		$C_e(\xi, t) \text{ [kg/m}^2/\text{s]}$	
	Min.	Max.	Min.	Max.	Min.	Max.	Min.	Max.
10^{-8}	2.3040×10^7	7.3732×10^7	6.6657×10^6	3.4600×10^7	0.4071	0.8842	0.9076	3.3377
10^{-7}	2.3429×10^6	7.3732×10^6	6.8106×10^5	3.4600×10^6	0.4098	0.8842	0.9076	3.3213
10^{-6}	2.7476×10^5	7.3732×10^5	8.3796×10^4	3.4600×10^5	0.4388	0.8842	0.9076	3.1548
10^{-5}	4.0799×10^4	1.2754×10^5	1.4492×10^4	8.0673×10^4	0.5509	1.7214	0.2704	1.7339

Table 2: Cartesian coordinates: Extrema of $h_s(T_s)$, $h_w(T_s, p_e)$, $B'(T_s, p_e)$, and $C_e(\xi, t)$ for $t \in [0, \bar{t}]$.

$\bar{\alpha} \text{ [m}^2/\text{s]}$	$h_r(\xi, t) \text{ [J/kg]}, \epsilon \neq 0$		$h_r(\xi, t) \text{ [J/kg]}, \epsilon = 0$	
	Min.	Max.	Min.	Max.
10^{-8}	1.2985×10^4	2.1250×10^5	6.0431×10^3	7.3901×10^4
10^{-7}	1.3267×10^4	2.1250×10^5	6.1212×10^3	7.3901×10^4
10^{-6}	1.6589×10^4	2.1250×10^5	6.9825×10^3	7.3901×10^4
10^{-5}	9.6647×10^4	4.7331×10^6	3.8625×10^4	5.6898×10^5

Table 3: Cartesian coordinates: Extrema of $h_r(\xi, t)$ for $t \in [0, \bar{t}]$.

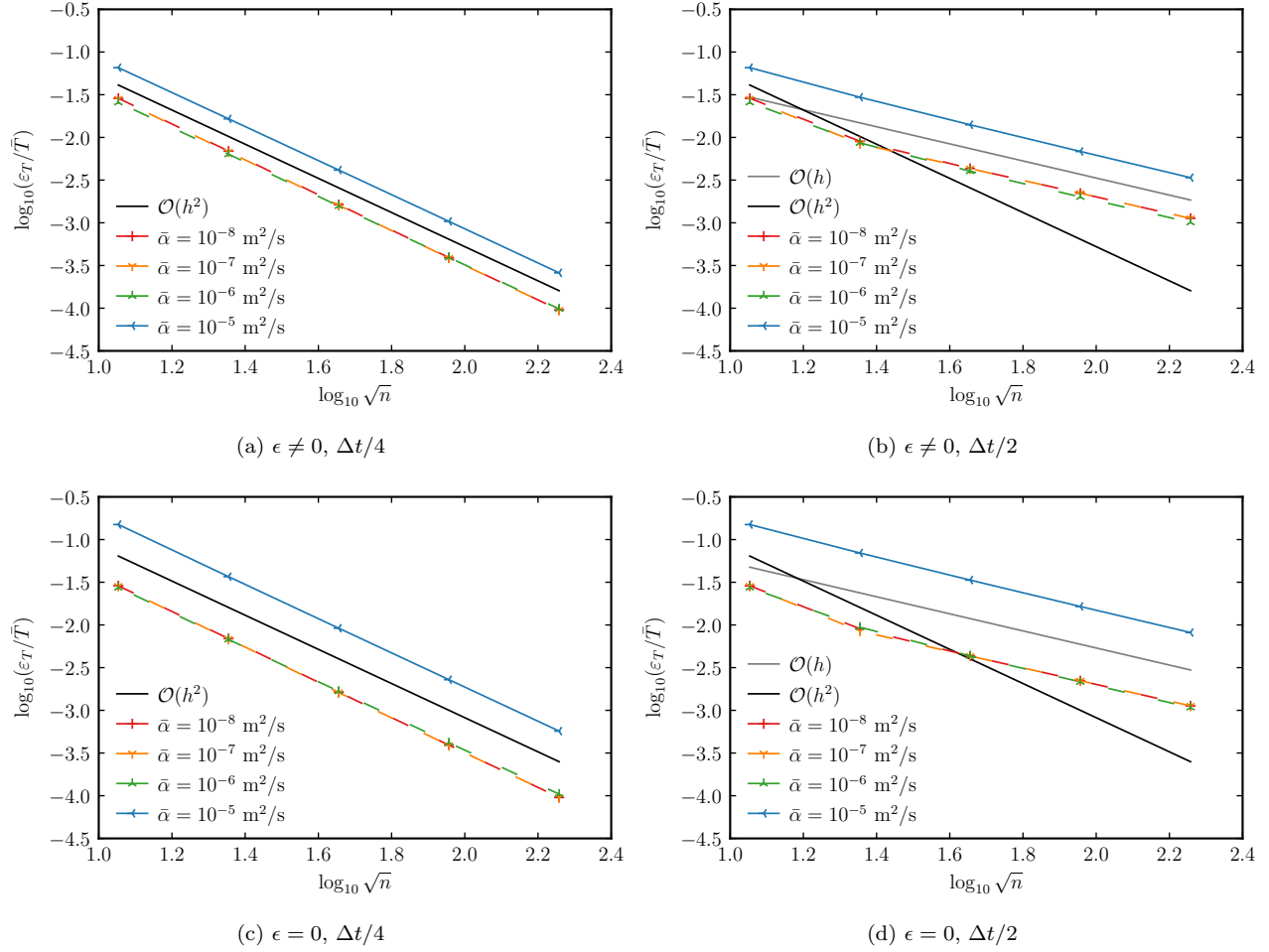


Figure 5: Cartesian coordinates: Norm of the error for T .

	Mesh	$\Delta t/4$, for $\bar{\alpha} [\text{m}^2/\text{s}]$				$\Delta t/2$, for $\bar{\alpha} [\text{m}^2/\text{s}]$			
		10^{-8}	10^{-7}	10^{-6}	10^{-5}	10^{-8}	10^{-7}	10^{-6}	10^{-5}
$\epsilon \neq 0$	1-2	2.0545	2.0588	2.0146	1.9901	1.6710	1.7444	1.5752	1.1496
	2-3	2.0832	2.0790	2.0152	1.9919	1.0589	0.9648	1.1002	1.0714
	3-4	2.0595	2.0492	2.0016	1.9979	0.9646	0.9602	1.0008	1.0372
	4-5	2.0361	2.0219	2.0015	2.0013	0.9755	0.9771	0.9919	1.0190
$\epsilon = 0$	1-2	2.0543	2.0600	2.0218	2.0265	1.6713	1.7545	1.5411	1.1061
	2-3	2.0838	2.0841	2.0122	2.0063	1.0601	0.9684	1.1190	1.0538
	3-4	2.0600	2.0531	2.0022	2.0017	0.9648	0.9604	1.0092	1.0272
	4-5	2.0366	2.0234	2.0001	2.0004	0.9755	0.9772	0.9951	1.0137

Table 4: Cartesian coordinates: Observed order of accuracy p for T .

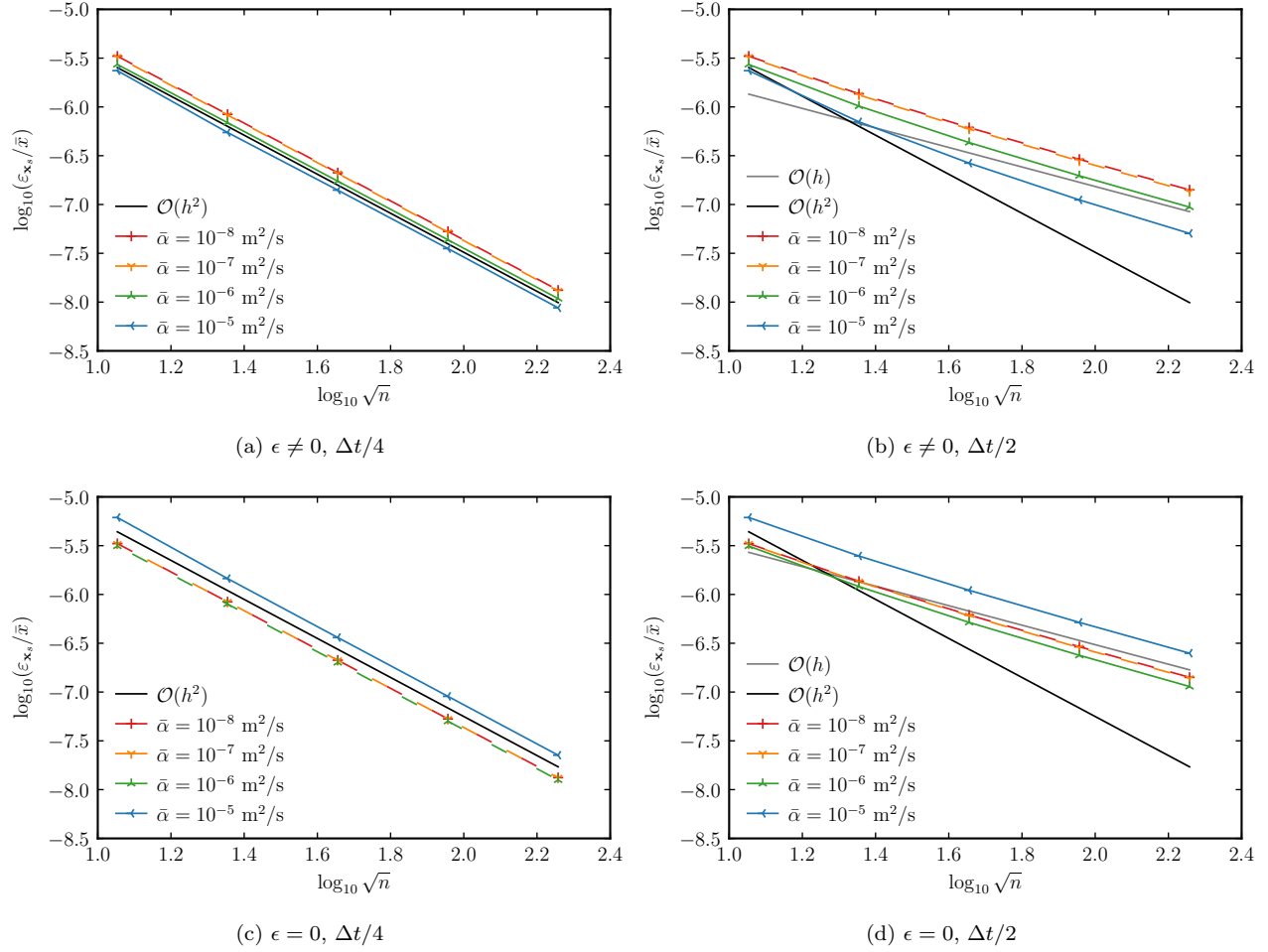


Figure 6: Cartesian coordinates: Norm of the error for \mathbf{x}_s .

	Mesh	$\Delta t/4$, for $\bar{\alpha} [\text{m}^2/\text{s}]$				$\Delta t/2$, for $\bar{\alpha} [\text{m}^2/\text{s}]$			
		10^{-8}	10^{-7}	10^{-6}	10^{-5}	10^{-8}	10^{-7}	10^{-6}	10^{-5}
$\epsilon \neq 0$	1-2	1.9809	1.9715	1.9796	2.1040	1.2825	1.2891	1.4152	1.7413
	2-3	1.9876	1.9883	1.9914	1.9620	1.1490	1.1591	1.2422	1.4057
	3-4	1.9983	1.9992	1.9975	1.9898	1.0799	1.0854	1.1302	1.2524
	4-5	1.9991	2.0002	2.0001	2.0169	1.0407	1.0435	1.0667	1.1405
$\epsilon = 0$	1-2	1.9809	1.9712	1.9744	2.0785	1.2822	1.2862	1.3775	1.3111
	2-3	1.9876	1.9881	1.9906	2.0079	1.1489	1.1572	1.2206	1.1667
	3-4	1.9983	1.9992	1.9974	2.0016	1.0798	1.0845	1.1198	1.0927
	4-5	1.9991	2.0001	2.0000	2.0037	1.0407	1.0431	1.0620	1.0491

Table 5: Cartesian coordinates: Observed order of accuracy p for \mathbf{x}_s .

negative. For $u_0(x)$, we choose an imaginary valued $\mu_0 = 3\sqrt{-1}/(2W)$, such that $\lambda_{i,j}$ from (25) is negative and the temperature increases with time. $u_0(x) = \cosh(3x/(2W))$ from (24) then provides sufficient variation with respect to x . We set $\hat{\theta}_{0,0_0} = 400$ K, and $\hat{\theta}_{0,1_0} = -100$ K. With these choices, (18) becomes

$$\theta(\mathbf{x}, t) = 100e^{22,500\bar{\alpha}t} (4 - e^{-2500\pi^2\bar{\alpha}t} \cos(\pi y/H)) \cosh(3x/(2W)) \text{ K}.$$

To manufacture the recession, we manufacture

$$\mathbf{x}_s(\xi, t) = \left\{ W \left(1 - \frac{t}{\bar{t}} \frac{1 + 2 \sin(\pi\xi/2)}{4} \right), H\xi \right\},$$

which has the initial condition $\mathbf{x}_s(\xi, 0) = \{W, \xi H\}$, such that the initial domain is a rectangle. ξ is related to \mathbf{x}_s by $\xi = y_s/H$. We set $W = 1$ cm and $H = 2$ cm. Figure 2 shows the evolution of the domain, and Figure 4 shows the evolution of T for $\bar{\alpha} = 10^{-5}$ m²/s. Tables 1 and 2 list the extrema of T_s , $c_p(T_s)$, $k(T_s)$, $h_s(T_s)$, $h_w(T_s, p_e)$, $B'(T_s, p_e)$, and $C_e(\xi, t)$ for $t \in [0, \bar{t}]$. Table 3 lists the extrema of $h_r(\xi, t)$ with ($\epsilon \neq 0$) and without ($\epsilon = 0$) the radiative flux. These tables provide a brief summary of the magnitudes of these quantities. Even though $T(\mathbf{x}, t)$ increases with time for a given \mathbf{x} , T_s may not necessarily do so, due to the motion of \mathbf{x}_s . For $\bar{\alpha} = 10^{-5}$ m²/s, the maximum value of T_s occurs when $t = \bar{t}$; for the other values of $\bar{\alpha}$, the maximum occurs when $t = 0$. Therefore, for the variables in Tables 1–3, one of the extrema is either constant or inversely proportional to $\bar{\alpha}$ for $\bar{\alpha} = \{10^{-8}, 10^{-7}, 10^{-6}\}$ m²/s.

We consider five discretizations, for which we double the number of elements in both spatial dimensions for each subsequent discretization. The coarsest discretization contains 8×16 elements, and the finest contains 128×256 elements. For the time discretization, we quarter the time step ($\Delta t/4$) and halve the time step ($\Delta t/2$) for each subsequent discretization. The coarsest discretization has a time step of 0.2 s, and the finest has a time step of 0.78125 ms for $\Delta t/4$ and 12.5 ms for $\Delta t/2$. Because the spatial discretization is second-order accurate and the time-integration scheme is first-order accurate, we expect to achieve $\mathcal{O}(h^2)$ for $\Delta t/4$ and $\mathcal{O}(h)$ for $\Delta t/2$. We additionally consider cases with and without the radiative flux.

For each of the five values of $\bar{\alpha}$ with ($\epsilon \neq 0$) and without ($\epsilon = 0$) the radiative flux, Figures 5 and 6 show how the error norms ε_T (31) and $\varepsilon_{\mathbf{x}_s}$ (32), which are nondimensionalized by $\bar{T} = 1$ K and $\bar{x} = 1$ m, vary with respect to n , which is the number of elements. Additionally, Tables 4 and 5 provide the observed order of accuracy p between discretization pairs. The error norms in both plots and tables are $\mathcal{O}(h^2)$ for $\Delta t/4$ and $\mathcal{O}(h)$ for $\Delta t/2$, as expected.

6.2. Polar Coordinates

The second problem set we consider uses polar coordinates. For this problem set, we use constant coefficients, such that $f(T) = 1$, and $T(\mathbf{x}, t) = \theta(\mathbf{x}, t)$.

For $\theta(\mathbf{x}, t)$, we truncate (18) to $\max i = 0$ and $\max j = 1$. We choose this truncation because, from (27), $v_0(\phi) = 1$ and $v_1(\phi) = \cos(\pi\phi/\bar{\phi})$ enable us to obtain variation with respect to ϕ without $\theta(\mathbf{x}, t)$ becoming negative. For $u_{0,0}(r)$ and $u_{0,1}(r)$ in (28), we choose $\lambda_{0,0} = \lambda_{0,1} = -22,500$ m⁻², so that the temperature increases with time. $u_{0,0}(r)$ and $u_{0,1}(r)$ provide sufficient variation with respect to r . We set $\hat{\theta}_{0,0_0} = 200$ K, and $\hat{\theta}_{0,1_0} = 30$ K.

To manufacture the recession, we relate ξ to \mathbf{x}_s by $\xi = \phi_s/\bar{\phi}$, and we manufacture

$$\mathbf{x}_s(\xi, t) = r_s(\xi, t) \{\cos \phi_s, \sin \phi_s\}, \quad (33)$$

where

$$r_s(\xi, t) = r_1 - (r_1 - r_0) \frac{t}{\bar{t}} \frac{3 + \cos(\pi\xi)}{8}.$$

Equation (33) has the initial condition $\mathbf{x}_s(\xi, 0) = r_1 \{\cos \phi_s, \sin \phi_s\}$, such that the initial domain is a fractional annulus. We set $r_0 = 1$ cm, $r_1 = 2$ cm, and $\bar{\phi} = \pi/2$. Figure 3 shows the evolution of the domain, and Figure 7 shows the evolution of T for $\bar{\alpha} = 10^{-5}$ m²/s. Tables 6 and 7 list the extrema of T_s , $c_p(T_s)$, $k(T_s)$, $h_s(T_s)$, $h_w(T_s, p_e)$, $B'(T_s, p_e)$, and $C_e(\xi, t)$ for $t \in [0, \bar{t}]$. Table 8 lists the extrema of $h_r(\xi, t)$ with ($\epsilon \neq 0$) and without ($\epsilon = 0$) the radiative flux. These tables provide a brief summary of the magnitudes of these

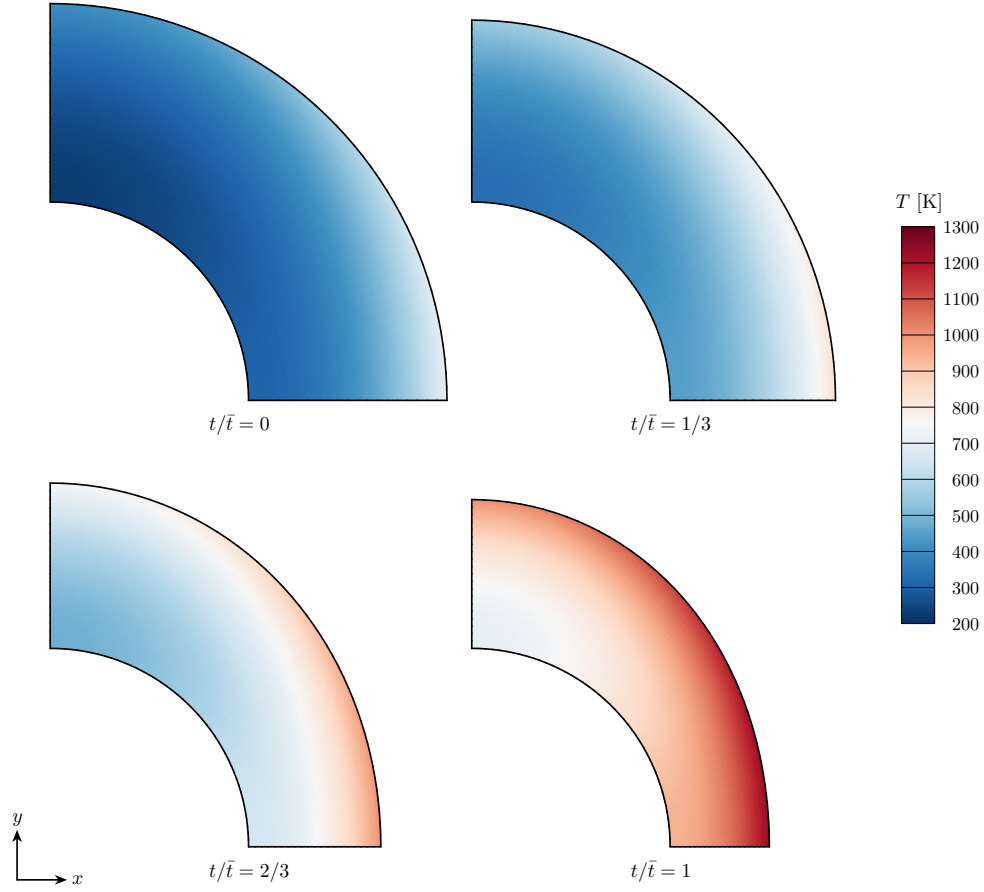


Figure 7: Polar coordinates: Temperature at multiple instances in time for $\bar{\alpha} = 10^{-5} \text{ m}^2/\text{s}$.

$\bar{\alpha} \text{ [m}^2/\text{s]}$	$T_s \text{ [}\times 10^3 \text{ K]}$		$c_p(T_s) \text{ [J/kg/K]}$		$k(T_s) \text{ [}\times 10^{-1} \text{ W/m/K]}$	
	Min.	Max.	Min.	Max.	Min.	Max.
10^{-8}	0.3268	0.6994	7.0000×10^4	7.0000×10^4	7.0000	7.0000
10^{-7}	0.3301	0.6994	7.0000×10^3	7.0000×10^3	7.0000	7.0000
10^{-6}	0.3653	0.6994	7.0000×10^2	7.0000×10^2	7.0000	7.0000
10^{-5}	0.4110	1.2353	7.0000×10^1	7.0000×10^1	7.0000	7.0000

Table 6: Polar coordinates: Extrema of T_s , $c_p(T_s)$, and $k(T_s)$ for $t \in [0, \bar{t}]$.

$\bar{\alpha} \text{ [m}^2/\text{s]}$	$h_s(T_s) \text{ [J/kg]}$		$h_w(T_s, p_e) \text{ [J/kg]}$		$B'(T_s, p_e) \text{ [}\times 10^{-1}]$		$C_e(\xi, t) \text{ [kg/m}^2/\text{s]}$	
	Min.	Max.	Min.	Max.	Min.	Max.	Min.	Max.
10^{-8}	3.7530×10^6	2.9834×10^7	8.0534×10^5	8.5613×10^6	2.7321	4.0245	1.6576	3.3967
10^{-7}	3.9858×10^5	2.9834×10^6	8.5752×10^4	8.5613×10^5	2.7412	4.0245	1.6576	3.3828
10^{-6}	6.4478×10^4	2.9834×10^5	1.4259×10^4	8.5613×10^4	2.8393	4.0245	1.6576	3.2397
10^{-5}	9.6514×10^3	6.7348×10^4	2.2366×10^3	2.7206×10^4	3.0164	6.7772	0.9285	2.4848

Table 7: Polar coordinates: Extrema of $h_s(T_s)$, $h_w(T_s, p_e)$, $B'(T_s, p_e)$, and $C_e(\xi, t)$ for $t \in [0, \bar{t}]$.

$\bar{\alpha}$ [m ² /s]	$h_r(\xi, t)$ [J/kg], $\epsilon \neq 0$		$h_r(\xi, t)$ [J/kg], $\epsilon = 0$	
	Min.	Max.	Min.	Max.
10^{-8}	7.9476×10^3	2.9082×10^4	7.6789×10^3	2.4335×10^4
10^{-7}	8.0748×10^3	2.9082×10^4	7.7888×10^3	2.4335×10^4
10^{-6}	9.5107×10^3	2.9082×10^4	8.9993×10^3	2.4335×10^4
10^{-5}	1.7725×10^4	1.4163×10^5	1.7095×10^4	6.6926×10^4

Table 8: Polar coordinates: Extrema of $h_r(\xi, t)$ for $t \in [0, \bar{t}]$.

quantities. For $\bar{\alpha} = 10^{-5}$ m²/s, the maximum value of T_s occurs when $t = \bar{t}$; for the other values of $\bar{\alpha}$, the maximum occurs when $t = 0$. Therefore, for the variables in Tables 6–8, one of the extrema is either constant or inversely proportional to $\bar{\alpha}$ for $\bar{\alpha} = \{10^{-8}, 10^{-7}, 10^{-6}\}$ m²/s.

We consider five discretizations, for which we double the number of elements in both spatial dimensions for each subsequent discretization. The coarsest discretization contains 8×18 elements, and the finest contains 128×288 elements. For the time discretization, we quarter the time step ($\Delta t/4$) and halve the time step ($\Delta t/2$) for each subsequent discretization. The coarsest discretization has a time step of 0.2 s, and the finest has a time step of 0.78125 ms for $\Delta t/4$ and 12.5 ms for $\Delta t/2$. Because the spatial discretization is second-order accurate and the time-integration scheme is first-order accurate, we expect to achieve $\mathcal{O}(h^2)$ for $\Delta t/4$ and $\mathcal{O}(h)$ for $\Delta t/2$. We additionally consider cases with and without the radiative flux.

For each of the five values of $\bar{\alpha}$ with ($\epsilon \neq 0$) and without ($\epsilon = 0$) the radiative flux, Figures 8 and 9 show how the error norms ε_T (31) and $\varepsilon_{\mathbf{x}_s}$ (32) vary with respect to n . Additionally, Tables 9 and 10 provide the observed order of accuracy p between discretization pairs. The error norms in both plots and tables are $\mathcal{O}(h^2)$ for $\Delta t/4$ and approach $\mathcal{O}(h)$ for $\Delta t/2$, as expected.

7. Conclusions

In this paper, we provided an approach to perform code verification for two-dimensional, non-decomposing ablation by deriving solutions that did not require code modification. Through this approach, we computed solutions to the heat equations for different coordinate systems, then we manufactured the dependencies of the boundary conditions. In doing so, we could compute error norms and measure their convergence rates.

We demonstrated this approach for two cases: one with a Cartesian coordinate system, and one with a polar coordinate system. For both cases, we considered different thermal diffusivity values to change the relative weights between the spatial and temporal contributions to the discretization error as we assessed its convergence rate. Both cases yielded the expected convergence rates given the discretization refinement ratios.

Acknowledgments

This paper describes objective technical results and analysis. Any subjective views or opinions that might be expressed in the paper do not necessarily represent the views of the U.S. Department of Energy or the United States Government. Sandia National Laboratories is a multimission laboratory managed and operated by National Technology and Engineering Solutions of Sandia, LLC, a wholly owned subsidiary of Honeywell International, Inc., for the U.S. Department of Energy’s National Nuclear Security Administration under contract DE-NA-0003525.

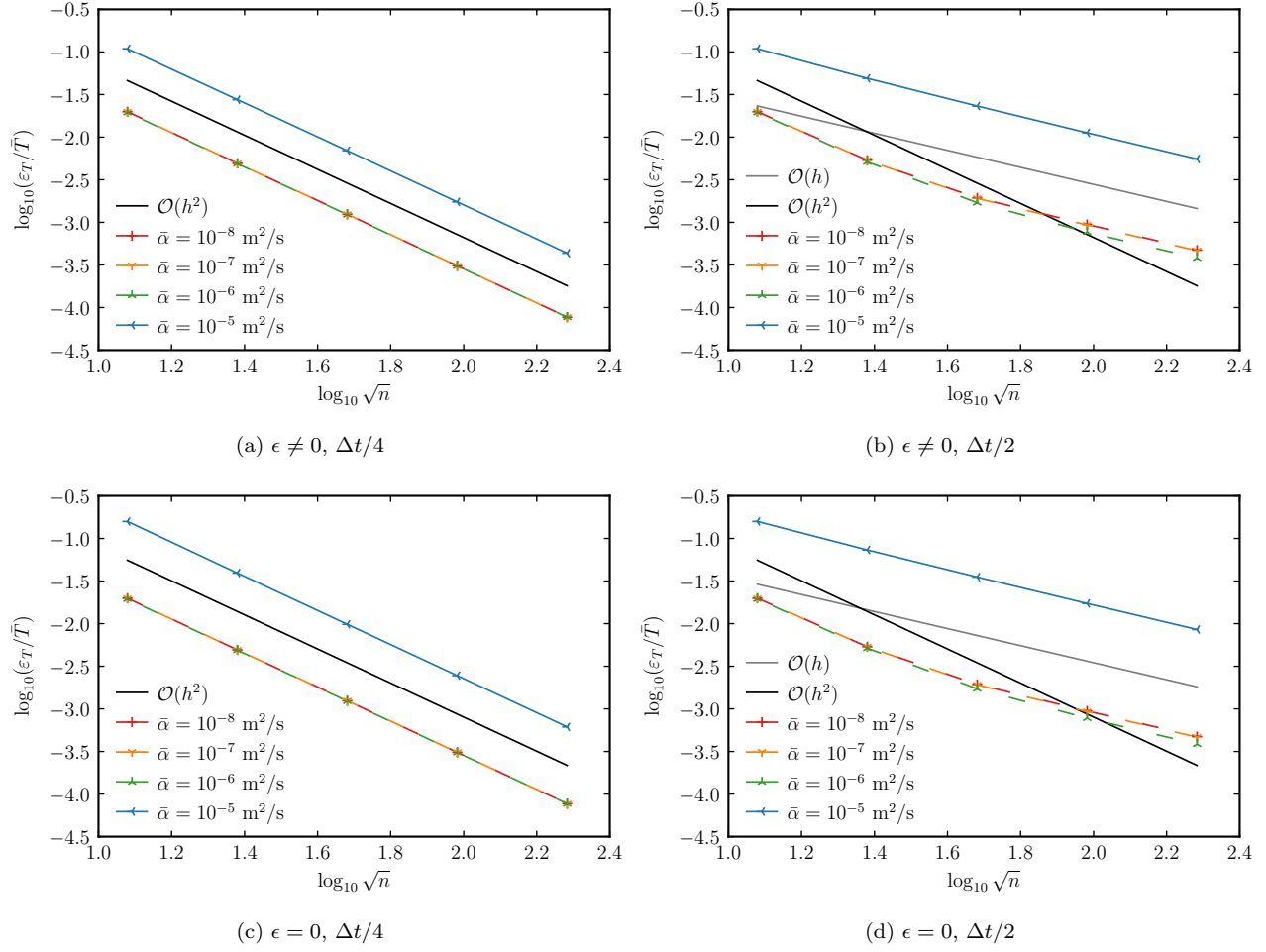


Figure 8: Polar coordinates: Norm of the error for T .

	Mesh	$\Delta t/4$, for $\bar{\alpha}$ [m ² /s]				$\Delta t/2$, for $\bar{\alpha}$ [m ² /s]			
		10^{-8}	10^{-7}	10^{-6}	10^{-5}	10^{-8}	10^{-7}	10^{-6}	10^{-5}
$\epsilon \neq 0$	1-2	2.0136	2.0120	1.9975	1.9834	1.8909	1.8932	1.9269	1.1528
	2-3	1.9836	1.9829	1.9848	1.9893	1.4691	1.4813	1.5894	1.0803
	3-4	2.0105	2.0092	2.0017	1.9982	1.0356	1.0394	1.1482	1.0432
	4-5	2.0019	2.0011	1.9990	1.9993	0.9995	0.9984	1.0124	1.0220
$\epsilon = 0$	1-2	2.0136	2.0123	1.9975	2.0120	1.8908	1.8926	1.9199	1.1108
	2-3	1.9836	1.9829	1.9844	1.9979	1.4692	1.4820	1.5808	1.0570
	3-4	2.0105	2.0093	2.0021	2.0002	1.0357	1.0395	1.1459	1.0303
	4-5	2.0019	2.0012	1.9989	1.9999	0.9995	0.9984	1.0120	1.0154

Table 9: Polar coordinates: Observed order of accuracy p for T .

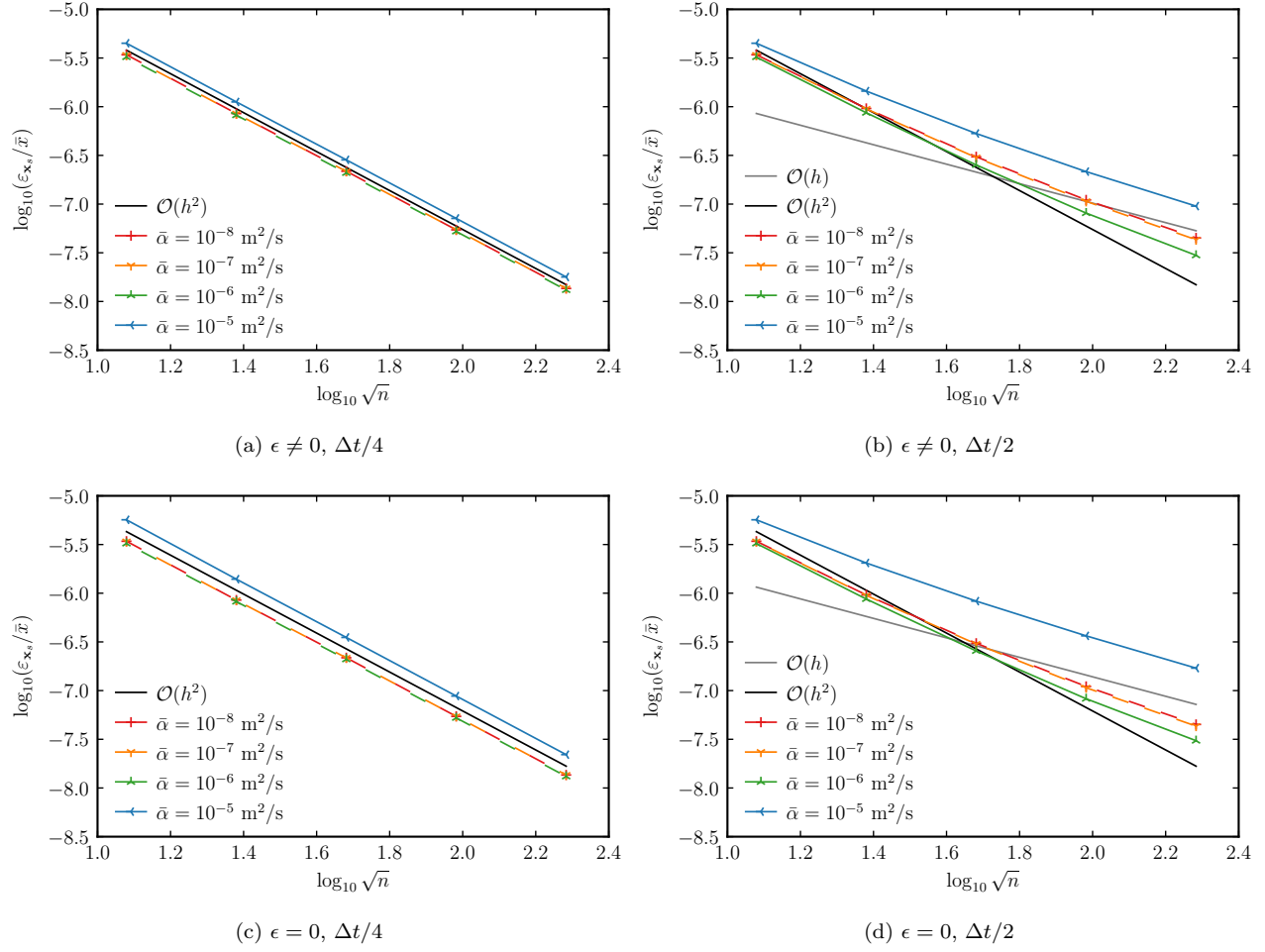


Figure 9: Polar coordinates: Norm of the error for \mathbf{x}_s .

	Mesh	$\Delta t/4$, for $\bar{\alpha}$ [m ² /s]				$\Delta t/2$, for $\bar{\alpha}$ [m ² /s]			
		10^{-8}	10^{-7}	10^{-6}	10^{-5}	10^{-8}	10^{-7}	10^{-6}	10^{-5}
$\epsilon \neq 0$	1-2	2.0061	2.0024	1.9817	2.0022	1.8325	1.8379	1.8983	1.6327
	2-3	1.9681	1.9655	1.9694	1.9763	1.6484	1.6581	1.7792	1.4466
	3-4	1.9993	1.9961	1.9964	1.9972	1.4723	1.4934	1.6427	1.3003
	4-5	1.9986	1.9985	1.9976	1.9982	1.2966	1.3097	1.4414	1.1767
$\epsilon = 0$	1-2	2.0062	2.0026	1.9818	2.0257	1.8325	1.8375	1.8938	1.4738
	2-3	1.9681	1.9655	1.9696	1.9874	1.6483	1.6572	1.7709	1.3011
	3-4	1.9993	1.9961	1.9964	1.9993	1.4722	1.4923	1.6313	1.1841
	4-5	1.9986	1.9985	1.9977	1.9989	1.2965	1.3088	1.4302	1.1011

Table 10: Polar coordinates: Observed order of accuracy p for \mathbf{x}_s .

Appendix A. Stability Implications of $\frac{\partial q_s}{\partial T_s}$

Consider the constant-coefficient heat equation (16). From (10) and (17), the boundary condition on Γ_0 is $\frac{\partial \theta}{\partial n} = 0$. From (9) and (17), the boundary condition on Γ_s is

$$-\bar{k} \frac{\partial \theta}{\partial n} = -k(T_s) \frac{\partial T}{\partial n} = q_s(T_s).$$

Consider two solutions to (16): θ and $\tilde{\theta}$. From (16), the difference $e_\theta = \tilde{\theta} - \theta$ is governed by

$$\frac{\partial e_\theta}{\partial t} - \bar{\alpha} \Delta e_\theta = 0. \quad (\text{A.1})$$

The boundary condition on Γ_0 is $\frac{\partial e_\theta}{\partial n} = 0$, and the boundary condition on Γ_s is

$$-\bar{k} \frac{\partial e_\theta}{\partial n} = q_s(\tilde{T}_s) - q_s(T_s). \quad (\text{A.2})$$

A Taylor series expansion of $q_s(\tilde{T}_s) - q_s(T_s)$ in (A.2) about $\tilde{T}_s = T_s$ yields

$$q_s(\tilde{T}_s) - q_s(T_s) = \frac{\partial q_s}{\partial T_s} e_{T_s} + \mathcal{O}(e_{T_s}^2), \quad (\text{A.3})$$

where $e_{T_s} = \tilde{T}_s - T_s$ and a Taylor series expansion of e_{T_s} about $\tilde{\theta}_s = \theta_s$ yields

$$e_{T_s} = F^{-1}(\tilde{\theta}_s) - F^{-1}(\theta_s) = \frac{1}{f(T_s)} e_{\theta_s} + \mathcal{O}(e_{\theta_s}^2). \quad (\text{A.4})$$

Therefore, from (A.2), (A.3), and (A.4), at Γ_s ,

$$-k(T_s) \frac{\partial e_\theta}{\partial n} = \frac{\partial q_s}{\partial T_s} e_{\theta_s} + \mathcal{O}(e_{\theta_s}^2). \quad (\text{A.5})$$

As in Section 4, we express the solution to (A.1) as

$$e_\theta(\mathbf{x}, t) = \sum_{i=0}^{\infty} \sum_{j=0}^{\infty} \hat{e}_{\theta_{i,j}}(t) \varphi_{i,j}(\mathbf{x}),$$

such that

$$\hat{e}_{\theta_{i,j}}(t) = \hat{e}_{\theta_{i,j0}} e^{-\bar{\alpha} \lambda_{i,j} t}. \quad (\text{A.6})$$

If $\lambda_{i,j}$ is negative in (A.6), e_θ will grow with time, introducing a bifurcation, unless $\varphi_{i,j}(\mathbf{x}) = 0$.

From (19),

$$\Delta \varphi_{i,j}(\mathbf{x}) + \lambda_{i,j} \varphi_{i,j}(\mathbf{x}) = 0, \quad (\text{A.7})$$

where the boundary condition on Γ_0 is $\frac{\partial \varphi_{i,j}}{\partial n} = 0$, and, from (A.5), the boundary condition on Γ_s is

$$-k(T_s) \frac{\partial \varphi_{i,j}}{\partial n} \approx \frac{\partial q_s}{\partial T_s} \varphi_{i,j}. \quad (\text{A.8})$$

Projecting (A.7) onto $\varphi_{i,j}(\mathbf{x})$ yields

$$\int_{\Omega(t)} \varphi_{i,j}(\mathbf{x}) \Delta \varphi_{i,j}(\mathbf{x}) d\Omega + \lambda_{i,j} \int_{\Omega(t)} \varphi_{i,j}(\mathbf{x})^2 d\Omega = 0. \quad (\text{A.9})$$

Integrating the first term in (A.9) by parts using (A.8) yields

$$-\int_{\Gamma_s(t)} \frac{1}{k(T_s)} \frac{\partial q_s}{\partial T_s} \varphi_{i,j}(\mathbf{x}_s)^2 d\Gamma - \int_{\Omega(t)} \|\nabla \varphi_{i,j}(\mathbf{x})\|^2 d\Omega + \lambda_{i,j} \int_{\Omega(t)} \varphi_{i,j}(\mathbf{x})^2 d\Omega = 0. \quad (\text{A.10})$$

In (A.10), if $\varphi_{i,j}(\mathbf{x}) \neq 0$, $\lambda_{i,j}$ will be positive if $\frac{\partial q_s}{\partial T_s} \geq 0$. Therefore, if $\frac{\partial q_s}{\partial T_s} \geq 0$, e_θ will not increase in time and the bifurcation will be avoided.

References

- [1] P. J. Roache, *Verification and Validation in Computational Science and Engineering*, Hermosa Publishers, 1998.
- [2] K. Salari, P. Knupp, Code verification by the method of manufactured solutions, Sandia Report SAND2000-1444, Sandia National Laboratories (Jun. 2000). [doi:10.2172/759450](https://doi.org/10.2172/759450).
- [3] W. L. Oberkampf, C. J. Roy, *Verification and Validation in Scientific Computing*, Cambridge University Press, 2010. [doi:10.1017/cbo9780511760396](https://doi.org/10.1017/cbo9780511760396).
- [4] C. J. Roy, Review of code and solution verification procedures for computational simulation, *Journal of Computational Physics* 205 (1) (2005) 131–156. [doi:10.1016/j.jcp.2004.10.036](https://doi.org/10.1016/j.jcp.2004.10.036).
- [5] P. J. Roache, Code verification by the method of manufactured solutions, *Journal of Fluids Engineering* 124 (1) (2001) 4–10. [doi:10.1115/1.1436090](https://doi.org/10.1115/1.1436090).
- [6] C. J. Roy, C. C. Nelson, T. M. Smith, C. C. Ober, Verification of Euler/Navier–Stokes codes using the method of manufactured solutions, *International Journal for Numerical Methods in Fluids* 44 (6) (2004) 599–620. [doi:10.1002/flid.660](https://doi.org/10.1002/flid.660).
- [7] R. B. Bond, C. C. Ober, P. M. Knupp, S. W. Bova, Manufactured solution for computational fluid dynamics boundary condition verification, *AIAA Journal* 45 (9) (2007) 2224–2236. [doi:10.2514/1.28099](https://doi.org/10.2514/1.28099).
- [8] S. Veluri, C. Roy, E. Luke, Comprehensive code verification for an unstructured finite volume CFD code, in: 48th AIAA Aerospace Sciences Meeting Including the New Horizons Forum and Aerospace Exposition, American Institute of Aeronautics and Astronautics, 2010. [doi:10.2514/6.2010-127](https://doi.org/10.2514/6.2010-127).
- [9] T. Oliver, K. Estacio-Hiroms, N. Malaya, G. Carey, Manufactured solutions for the Favre-averaged Navier–Stokes equations with eddy-viscosity turbulence models, in: 50th AIAA Aerospace Sciences Meeting including the New Horizons Forum and Aerospace Exposition, American Institute of Aeronautics and Astronautics, 2012. [doi:10.2514/6.2012-80](https://doi.org/10.2514/6.2012-80).
- [10] L. Eça, C. M. Klaij, G. Vaz, M. Hoekstra, F. Pereira, On code verification of RANS solvers, *Journal of Computational Physics* 310 (2016) 418–439. [doi:10.1016/j.jcp.2016.01.002](https://doi.org/10.1016/j.jcp.2016.01.002).
- [11] B. A. Freno, B. R. Carnes, V. G. Weirs, Code-verification techniques for hypersonic reacting flows in thermochemical nonequilibrium, *Journal of Computational Physics* 425 (2021). [doi:10.1016/j.jcp.2020.109752](https://doi.org/10.1016/j.jcp.2020.109752).
- [12] É. Chamberland, A. Fortin, M. Fortin, Comparison of the performance of some finite element discretizations for large deformation elasticity problems, *Computers & Structures* 88 (11) (2010) 664 – 673. [doi:10.1016/j.compstruc.2010.02.007](https://doi.org/10.1016/j.compstruc.2010.02.007).
- [13] S. Étienne, A. Garon, D. Pelletier, Some manufactured solutions for verification of fluid–structure interaction codes, *Computers & Structures* 106–107 (2012) 56–67. [doi:10.1016/j.compstruc.2012.04.006](https://doi.org/10.1016/j.compstruc.2012.04.006).
- [14] A. Veeraragavan, J. Beri, R. J. Gollan, Use of the method of manufactured solutions for the verification of conjugate heat transfer solvers, *Journal of Computational Physics* 307 (2016) 308–320. [doi:10.1016/j.jcp.2015.12.004](https://doi.org/10.1016/j.jcp.2015.12.004).
- [15] P. T. Brady, M. Herrmann, J. M. Lopez, Code verification for finite volume multiphase scalar equations using the method of manufactured solutions, *Journal of Computational Physics* 231 (7) (2012) 2924–2944. [doi:10.1016/j.jcp.2011.12.040](https://doi.org/10.1016/j.jcp.2011.12.040).
- [16] S. Lovato, S. L. Toxopeus, J. W. Settels, G. H. Keetels, G. Vaz, Code verification of non-Newtonian fluid solvers for single- and two-phase laminar flows, *Journal of Verification, Validation and Uncertainty Quantification* 6 (2) (2021). [doi:10.1115/1.4050131](https://doi.org/10.1115/1.4050131).

- [17] R. G. McClarren, R. B. Lowrie, Manufactured solutions for the p_1 radiation-hydrodynamics equations, *Journal of Quantitative Spectroscopy and Radiative Transfer* 109 (15) (2008) 2590–2602. [doi:10.1016/j.jqsrt.2008.06.003](https://doi.org/10.1016/j.jqsrt.2008.06.003).
- [18] J. R. Ellis, C. D. Hall, Model development and code verification for simulation of electrodynamic tether system, *Journal of Guidance, Control, and Dynamics* 32 (6) (2009) 1713–1722. [doi:10.2514/1.44638](https://doi.org/10.2514/1.44638).
- [19] R. G. Marchand, The method of manufactured solutions for the verification of computational electromagnetic codes, phdthesis, Stellenbosch (Mar. 2013).
- [20] B. A. Freno, N. R. Matula, W. A. Johnson, Manufactured solutions for the method-of-moments implementation of the electric-field integral equation, *Journal of Computational Physics* 443 (2021). [doi:10.1016/j.jcp.2021.110538](https://doi.org/10.1016/j.jcp.2021.110538).
- [21] B. A. Freno, N. R. Matula, J. I. Owen, W. A. Johnson, Code-verification techniques for the method-of-moments implementation of the electric-field integral equation, *Journal of Computational Physics* 451 (2022). [doi:10.1016/j.jcp.2021.110891](https://doi.org/10.1016/j.jcp.2021.110891).
- [22] R. Hogan, B. Blackwell, R. Cochran, Numerical solution of two-dimensional ablation problems using the finite control volume method with unstructured grids, in: 6th AIAA/ASME Joint Thermophysics and Heat Transfer Conference, no. AIAA 1994-2085, American Institute of Aeronautics and Astronautics, 1994. [doi:10.2514/6.1994-2085](https://doi.org/10.2514/6.1994-2085).
- [23] B. F. Blackwell, R. E. Hogan, One-dimensional ablation using Landau transformation and finite control volume procedure, *Journal of Thermophysics and Heat Transfer* 8 (2) (1994) 282–287. [doi:10.2514/3.535](https://doi.org/10.2514/3.535).
- [24] A. J. Amar, B. F. Blackwell, J. R. Edwards, One-dimensional ablation using a full Newton’s method and finite control volume procedure, *Journal of Thermophysics and Heat Transfer* 22 (1) (2008) 71–82. [doi:10.2514/1.29610](https://doi.org/10.2514/1.29610).
- [25] A. J. Amar, B. F. Blackwell, J. R. Edwards, Development and verification of a one-dimensional ablation code including pyrolysis gas flow, *Journal of Thermophysics and Heat Transfer* 23 (1) (2009) 59–71. [doi:10.2514/1.36882](https://doi.org/10.2514/1.36882).
- [26] A. Amar, N. Calvert, B. Kirk, Development and verification of the charring ablating thermal protection implicit system solver, in: 49th AIAA Aerospace Sciences Meeting including the New Horizons Forum and Aerospace Exposition, 2011. [doi:10.2514/6.2011-144](https://doi.org/10.2514/6.2011-144).
- [27] B. A. Freno, B. R. Carnes, N. R. Matula, Nonintrusive manufactured solutions for ablation, *Physics of Fluids* 33 (1) (2021). [doi:10.1063/5.0037245](https://doi.org/10.1063/5.0037245).
- [28] M. Abramowitz, I. A. Stegun, Handbook of mathematical functions with formulas, graphs, and mathematical tables, Vol. 55, United States Department of Commerce, National Bureau of Standards, 1964.
- [29] SIERRA Thermal/Fluid Development Team, SIERRA multimechanics module: Aria user manual – version 4.56, Sandia Report SAND2020-4000, Sandia National Laboratories (Apr. 2020). [doi:10.2172/1615880](https://doi.org/10.2172/1615880).
- [30] A. N. Gent, A new constitutive relation for rubber, *Rubber Chemistry and Technology* 69 (1) (1996). [doi:10.5254/1.3538357](https://doi.org/10.5254/1.3538357).